SHOULD HYDRODYNAMICS BE TAKEN INTO ACCOUNT WHEN CALCULATING THE GROWTH RATE OF MICROALGAE IN A PHOTOBIOREACTOR ?

J. IGNACIO FIERRO U., LIU-DI LU, OLIVIER BERNARD

Abstract. Microalgae, as photosynthetic organisms, are cultivated in photobioreactors for various industrial applications. Light intensity, a critical factor influencing their growth rate, is inherently non-uniform within photobioreactors. In regions distant from the illuminated surface, microalgae experience photolimitation due to insufficient photon availability, hindering optimal activation of the photosynthetic machinery. Conversely, near the illuminated surface, excessive light intensity can damage key photosynthetic proteins, leading to photoinhibition. While mixing in photobioreactors does not alter the light gradient, it influences the light exposure history of cells through hydrodynamic advection. In this study, we employ Han's mechanistic model to describe the dynamics of photon harvesting and its consequences, including photoinhibition and photolimitation. First, we calculate the time-averaged growth rate for arbitrary continuous light signals, revealing how mixing impacts growth under the assumption of periodic light signals generated by hydrodynamics. Next, we address the computational challenge of estimating growth rates in photobioreactors using computational fluid dynamics (CFD), modeling a single-phase incompressible fluid. Finally, we analyze the case of a raceway pond, evaluating errors arising when growth rate is estimated without accounting for hydrodynamics. We analytical demonstrate that the gain in growth is related to the cell movement along the light gradient. Our results show that in predominantly laminar hydrodynamic regimes, hydrodynamics has only a marginal effect on microalgal growth. Moreover, we show that the average productivity can be estimated based on a static approximation of the average growth rate taking into account the light distribution, with an error lower than 10%.

Key words. microalgae, mixing, computational fluid dynamics, raceway pond, Han model.

MSC codes. 92B99, 34A05, 34C25, 34A34, 76B07

1. Introduction. Microalgae are capable of converting CO_2 into biomass using energy from visible light. These microorganisms are cultivated industrially in either open or closed photobioreactors [19]. Open systems such as raceway ponds are simple and cost-effective, shallow, oval-shaped channels, mixed with a paddle wheel. Closed systems, like tubular reactors, represent more advanced technology with more controlled culturing conditions. These reactors can operate in batch mode or with continuous addition of growth medium. Two key characteristics define these systems: (1) microalgae cells act as light-absorbing particles, creating a heterogeneous light distribution within the reactor. Areas near the light source experience high illumination, while deeper regions remain in darkness. (2) Intensive mixing is employed to prevent biomass sedimentation and ensure uniform nutrient distribution. As a result, cells are advected through light gradients, experiencing alternating periods of high and low light intensity.

Photon harvesting in microalgae is a dynamic process, and the average growth rate in a photobioreactor emerges from the complex interplay between photosystem dynamics and hydrodynamics [7]. Accurately modeling this interaction is challenging, as it requires accurate representation of 1/ reactor hydrodynamics, 2/ light distribution within the reactor, 3/ dynamic response of photon harvesting in response to light variations. This approach, which explicitly accounts for the light history of cells, is classified as type III in [3]. However, the complexity of type III models often limits their practical application, leading to the use of simplified growth rate (μ) calculations. Type I models depend solely on incident light at the reactor surface, while type II models incorporate simple light transfer models like the Lambert–Beer law, coupled with Monod-like or Haldane-type functions for $\mu(I)$. Unlike type I and II

models, which are static, type III models are dynamic.

Photosystem dynamics are typically described by three-population models, such as the Han model [14] or the Eilers–Peeters model [11]. These models use three differential equations to represent the probability of the photosystem being in one of three states: open and ready to process photons, closed and processing photons, or damaged due to excess light energy. These models capture two key phenomena—photoabsorption and photoinhibition—which operate on different timescales. The recovery rate after damage is significantly slower than photon harvesting, enabling a slow-fast approximation in the three-population model [15].

Cells in photobioreactor are exposed to continuous, fluctuating light signals over time resulting from their trajectories in the light gradient. In practice, they are most of the time exposed to suboptimal light conditions, reducing photosynthetic efficiency. Recent studies have explored optimizing light absorption in these reactors, by introducing specific topographies [5] or enhancing vertical mixing [6].

Using the Han model, we investigate the impact of fluctuating light signals on growth rates. By considering the typical timescales of light variations, we simplify the Han model using a slow-fast approximation and compare its predictions with those assuming steady-state photosystems. We first apply our coupled model to simple periodic light signals, commonly used in laboratory-scale photobioreactors. Then, we reconstruct the cell trajectories in a raceway pond using computational fluid dynamics (CFD) simulations. The trajectories of the cells in the light gradient provide realistic light patterns whose effect on photosynthesis can be assessed using Han's model.

This paper is organized as follows. We first present the hydrodynamic and biological models in Section 2, where we compare two strategies for computing the growth rate: μ_A is a more realistic computation accounting for the dynamics of the photosystems, and μ_S is an approximation easier to compute assuming a static response of the photosynthetic apparatus. The main results of this paper, is a characterization of the relationship between the dynamic growth rate (μ_A) and the static approximation (μ_S). To better understand this relationship, we provide theoretical analysis in Section 3 and study the impact of continuous periodic light signals. We demonstrate that all solutions of the biological model converge to a unique periodic solution. Numerical studies are provided in Section 4, where we first illustrate the mixing in a photobioreactor using two typical periodic light signals. We then analyze the raceway pond using a CFD model to simulate the motion of particles, tracking the light perceived by individual microalgae. We compare the actual average growth rate and the static approximation by taking space into account. A detailed discussion is given in Section 5, where we comment our results and their applications on the design of photobioreactors. Finally, we conclude by demonstrating that the average growth rate computed assuming the steady state of the photosystems is a reliable approximation.

2. Hydrodynamic and biological models.

2.1. Computational fluid dynamic model model and cell tracking. The water flow in a raceway pond can be simulated with CFD, which integrates the Navier–Stokes equations. Several studies have used CFD to simulate the velocity field in open ponds [25, 27]. Lagrangian approaches have also been used to assess the mixing efficiency in algae cultures. For example, the mixing length is computed in [1] as a result of different paddle wheel velocities. In our study, we consider a real raceway pond from the Environmental Biotechnology Laboratory of INRAE Narbonne in France [17]. We use a layer-averaged Euler and Navier–Stokes model for the numerical simulation of incompressible free surface, as presented in [2]. The meshing of the raceway pond
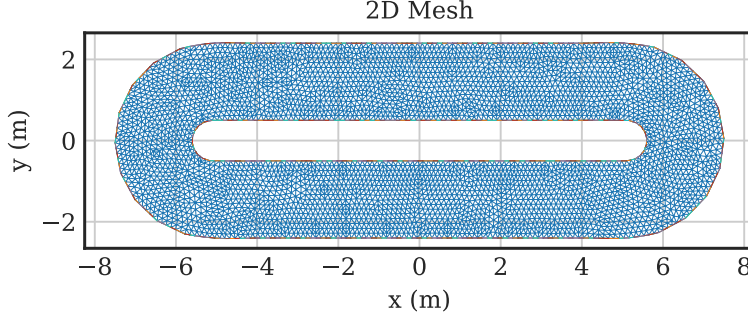
2

Fig. 2.1: 2D mesh of the simulated raceway pond.

99   consists of a fixed 2D triangular mesh of the bottom of the raceway, as shown in Fig-
100 ure 2.1. The layers are defined by the water depth, giving the third dimension of the
101 system.   This approximation of the Navier–Stokes equations is more accurate than
102 the well-known shallow water system. It employs a multi-layered model based on a
103 Galerkin-type approximation of the velocity field, utilizing piecewise constant basis
104 functions. A decisive advantage for raceway ponds is also that this discretization of
105 Navier–Stokes equations represents the free surface (and the waves) more simply, yet
106 more accurately than the classical approaches. The incompressible and hydrostatic
107 Navier–Stokes system with free surface is given by

$$\nabla \cdot \boldsymbol{U} = 0,$$

108 (2.1)
$$\frac{\partial \boldsymbol{u}}{\partial t} + \nabla_{x,y} \cdot (\boldsymbol{u} \otimes \boldsymbol{u}) + \frac{\partial \boldsymbol{u} w}{\partial z} = \frac{1}{\rho_0} \nabla_{x,y} \cdot \sigma + \frac{\mu}{\rho_0} \frac{\partial^2 \boldsymbol{u}}{\partial z^2} + \boldsymbol{F},$$

$$\frac{\partial p}{\partial z} = -\rho_0 g,$$

109 where $\boldsymbol{U} = (u, v, w)^T$ is the velocity of the liquid, $\boldsymbol{u} = (u, v)^T$ is the horizontal veloc-
110 ity, σ is $-p I_d + \Sigma$, where $\Sigma = \mu \nabla_{x,y} \boldsymbol{u}$ is the total stress tensor, p is the pressure, g is
111 the gravity acceleration constant, ρ_0 is the fluid density and μ is the viscosity coeffi-
112 cient. The fluid is assumed to be Newtonian. The hydrostatic Navier–Stokes system
113 is relevant here, since vertical acceleration is negligible compared to the horizontal
114 acceleration. The paddle wheel is indirectly represented by the force $\boldsymbol{F}$ as used in [4],

115 (2.2)
$$\boldsymbol{F} = F \left(\sqrt{(x - x_{\text{wheel}})^2 + (z - z_{\text{wheel}})^2} \omega \right)^2 \begin{pmatrix} \cos(\theta) \\ 0 \\ \sin(\theta) \end{pmatrix},$$

116 where F is a constant, θ is the angle between the vertical axis and the blade, $\omega = \dot{\theta}$, and
117 $x_{\text{wheel}}, z_{\text{wheel}}$ are the coordinates of the paddle wheel in the x and z axis respectively.
118 Note that the force does not affect the y-axis, which is parallel to the central axis of
119 the paddle wheel. It has been shown that using a 2D (horizontal and vertical axis)
120 representation of the raceway hydrodynamics [4] is computationally more efficient
121 than using model (2.1)-(2.2).
122   The fluid domain along the z-axis is delimited by the free surface denoted by
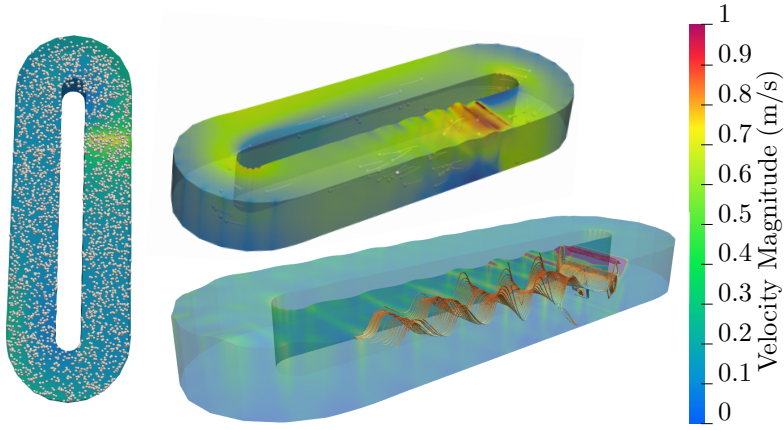
3

Fig. 2.2: Representation of a simulated raceway pond and the velocity field of some particles. The height corresponds to 0.3 (m). **Left:** Simulated particles representation (paddle wheel simulated at 12.5 RPM). **Top Right:** Lagrangian tracers of few particles (paddle wheel simulated at 20 RPM). **Bottom Right:** The streamline of some particles' trajectories (paddle wheel simulated at 15 RPM).

$\eta(t, x, y)$, then the system (2.1) is completed with the following boundary condition:

$$(2.3) \qquad \frac{\partial \eta}{\partial t} + \boldsymbol{u} \cdot \nabla_{x,y}\eta = 0.$$

The CFD model was validated in [2] using a velocity sensor in a smaller raceway pond. Our simulations are very similar to the one in [17], carried out with a commercial software, where a physical model of the paddle wheel was implemented.

We assume that the microalgae have the same density as the medium, so that the trajectories of the cells match that of the background flow. Under this hypothesis, Lagrangian's trajectories of these particles can be reconstructed from the Eulerian description (2.1) denoted by $(\boldsymbol{X}_n)_{i=1}^{N_{\mathrm{par}}}$, where N_{par} is the number of simulated particles. The position of each particle $\boldsymbol{X}_n(t) = (x_n, y_n, z_n)^T$ is computed by solving the equation

$$(2.4) \qquad \frac{\mathrm{d}\boldsymbol{X}_n(t)}{\mathrm{d}t} = \boldsymbol{U}(t), \quad \boldsymbol{X}_n(0) = (x_{n0}, y_{n0}, z_{n0})^T,$$

where (x_{n0}, y_{n0}, z_{n0}) is the initial position of the particle. We denote by Ω the domain of the raceway. We initiate the position of the particles randomly, following a uniform distribution in the domain Ω.

Similar works on the same pond [16, 23] have considered a growth model tracking the position of Lagrangian trajectories, using the same model (2.1), (2.2), and (2.4). In our study, we have considerably improved the numerical schemes, so that much more particle trajectories could be simulated with a higher accuracy. In particular, it is challenging to reproduce with the simulation the expected equidistribution of the cells along time, and much of the biases appeared in previous schemes were reduced. To illustrate this photobioreactor, we show a simulated raceway pond in Figure 2.2 together with the distribution of the velocity magnitude. The paddle wheel is positioned just above the red surface. Some cells (in white) are represented together with
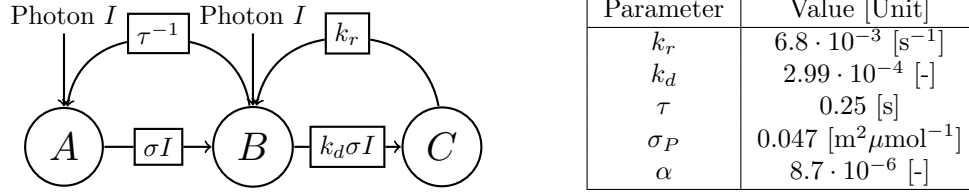
4

Fig. 2.3: **Left:** Illustration of the evolution between the three states in the Han model. **Right:** Parameters of the Han model used in this study.

Parameter	Value [Unit]
k_r	$6.8 \cdot 10^{-3}$ [s^{-1}]
k_d	$2.99 \cdot 10^{-4}$ [-]
τ	0.25 [s]
σ_P	0.047 [m$^2\mu$mol^{-1}]
α	$8.7 \cdot 10^{-6}$ [-]

147 their respective streamlines. The trajectories of the cells are mainly horizontal in the
148 straight sections of the raceway pond.

149 **2.2. Light distribution within the raceway pond.** We assume that a pop-
150 ulation of microalgae cells, each with a radius of 10 (μm), follows fluid streamlines
151 within the light gradient. Due to the incompressibility of the fluid and the cells' den-
152 sity being equal to that of the medium, the particles are, in theory, uniformly distrib-
153 uted throughout the raceway. This assumption justifies the use of the Lambert–Beer
154 law to approximate the light distribution, taking into account the scattering and ab-
155 sorption effects of the cells. The vertical motion of the cells in the light gradient can
156 therefore provide the individual light history of each cell. We assume that light strikes
157 perpendicularly to the ground surface. To reach a cell $\boldsymbol{X}_n$, the light must travel a
158 distance $\eta(t, x_n, y_n) - z_n$, from the free surface. Then the light signal I_n perceived by
159 this particle is computed with the Lambert–Beer law as

160 (2.5)
$$I_n(t) = I_0 e^{-\xi(\eta(t,x_n,y_n)-z_n)},$$

161 where I_0 is the light perceived at the free surface, $\xi > 0$ is the light extinction constant.

162 **2.3. Biological model.** To describe how photons are harvested by the photosys-
163 tems under a varying light intensity, we consider the mechanistic model of Han [14],
164 which characterizes the process of photon harvesting with possible photoinhibition
165 induced by the photodamage of the photosystem II (PSII). There are three possible
166 states for PSII: open or reactive state A, closed or activated state B, and inhibited
167 or damaged state C. The relation of these three states are schematically presented in
168 Figure 2.3. The dynamics of PSII can be described by the differential equations:

169 (2.6) $\dfrac{\mathrm{d}A}{\mathrm{d}t} = -I\sigma_P A + \dfrac{B}{\tau}, \ \dfrac{\mathrm{d}B}{\mathrm{d}t} = I\sigma_P A - \dfrac{B}{\tau} + k_r C - k_d \sigma_P I B, \ \dfrac{\mathrm{d}C}{\mathrm{d}t} = -k_r C + k_d \sigma_P I B,$

170 where σ_P (μmol^{-1}m^2) is the effective cross-section of PSII, I (μmolm^{-2}s^{-1}) is the
171 light intensity perceived by the microalgae, τ (s) is the minimal time required for
172 an electron to transfer from water on the donor side of the photosynthetic unit to
173 the terminal electron acceptors, which is also called the turnover time, k_d ($-$) is the
174 damage rate and k_r (s^{-1}) is the recovery rate of PSII. A, B and C represent the
175 probability distribution of each state, therefore

176 (2.7)
$$A + B + C = 1.$$

177 The algal growth rate is assumed to be proportional to the open state A and the
178 light intensity I. More precisely, the growth rate given by the kinetic model (2.6)

5

corresponds to

$$\mu_A(I, A) := \alpha \sigma_P I A, \tag{2.8}$$

where α is a constant of proportionality relating the flux of electrons triggered by the photons and cell growth. At steady state, the state A of the system (2.6) tends towards A_S (see, e.g., [7]). This corresponds exactly to a Haldane model where the growth rate is a function of light, that is

$$\mu_S(I) = \alpha \sigma_P I A_S = \alpha \sigma_P I \frac{1}{1 + \tau \sigma_P I + \frac{k_d}{k_r} \tau (\sigma_P I)^2}. \tag{2.9}$$

The maximum of μ_S is given by $\mu_{\max} = \frac{\alpha}{\tau + 2\sqrt{\frac{k_d}{k_r}\tau}}$, and it is reached when the light intensity value is

$$I_{\mathrm{opt}} = \frac{1}{\sigma_P \sqrt{\frac{k_d}{k_r}\tau}}. \tag{2.10}$$

As shown in [12], using (2.7) and substituting it into the system (2.6), we end up with two equations

$$\begin{aligned}
\frac{\mathrm{d}A}{\mathrm{d}t} &= -\left(\sigma_P I + \frac{1}{\tau}\right)A - \frac{1}{\tau}C + \frac{1}{\tau}, \\
\frac{\mathrm{d}C}{\mathrm{d}t} &= k_d\left[-\sigma_P I A - \left(\sigma_P I + \frac{k_r}{k_d}\right)C + \sigma_P I\right].
\end{aligned} \tag{2.11}$$

In practice, the factor k_d is in the range of 10^{-4}, as shown in Figure 2.3. Therefore, system (2.11) has slow/fast timescales, and we can consider the slow manifold proposed in [18, Chapter 11], where A rapidly reaches a pseudo steady state depending on the value of C:

$$A = \frac{1-C}{1+\tau\sigma_P I}, \tag{2.12}$$

This reduces the system (2.11) to a single equation of C,

$$\frac{\mathrm{d}C}{\mathrm{d}t} = -(\gamma(I) + k_r)C + \gamma(I), \tag{2.13}$$

with $\gamma(I) := \frac{k_d \tau (\sigma_P I)^2}{1 + \tau \sigma_P I}$. In particular, the steady state of C is given by $C_S := \frac{\gamma(I)}{\gamma(I) + k_r} = \frac{\frac{k_d}{k_r}\tau(\sigma_P I)^2}{1 + \tau\sigma_P I + \frac{k_d}{k_r}\tau(\sigma_P I)^2}$. Consequently, the steady state of A can be obtained by substituting C_S into (2.12).

For a continuous bounded light signal $I : [0, +\infty) \to [I_{\min}, I_{\max}]$ with $0 \le I_{\min} \le I_{\max}$, we present an estimation of the actual growth rate μ_A as a function of the static approximation μ_S assuming the Han model in equilibrium. To simplify the notation, we write $\mu_A(t)$ instead of $\mu_A(I(t), A(A(0); t))$ and $\mu_S(t)$ instead of $\mu_S(I(t))$. We now demonstrate that the initial condition rapidly does not affect the dynamics anymore and can therefore be neglected after a time interval of $10/k_r$ (about 25 minutes), much smaller than the typical timescale of growth.

6

PROPOSITION 2.1. *Let $I : [0, +\infty) \to [I_{\min}, I_{\max}]$ be a continuous bounded light signal. Assuming that $A(0) = 0$, the growth rate μ_A can be written as*

$$(2.14) \qquad \mu_A(t) = \mu_S(t)(\gamma(I(t)) + k_r) \int_0^t e^{-\int_s^t \gamma(I(w)) + k_r \, \mathrm{d}w} \, \mathrm{d}s.$$

Furthermore, the following estimations hold

$$(2.15) \qquad \mu_S(t) \frac{\gamma(I(t)) + k_r}{\gamma(I_{\max}) + k_r} \left(1 - e^{-(\gamma(I_{\max}) + k_r)t}\right) \leq \mu_A(t) \leq \mu_S(t) \frac{\gamma(I(t)) + k_r}{\gamma(I_{\min}) + k_r}.$$

In general, for any initial condition $A(0) = A_0$, the associated growth rate converges to (2.14) when t goes to infinity.

Proof. The general solution of (2.13) is given by

$$(2.16) \qquad C(t) = C(0)e^{-\int_0^t \gamma(I(w)) + k_r \, \mathrm{d}w} + \int_0^t \gamma(I(s))e^{-\int_s^t \gamma(I(w)) + k_r \, \mathrm{d}w} \, \mathrm{d}s.$$

Using then (2.12), the state A can be written as

$$
\begin{aligned}
(2.17) \qquad A(A(0); t) = {} & A(0) \frac{1 + \tau \sigma_P I(0)}{1 + \tau \sigma_P I(t)} e^{-\int_0^t \gamma(I(w)) + k_r \, \mathrm{d}w} \\
& + A_S(t)(\gamma(I(t)) + k_r) \int_0^t e^{-\int_s^t \gamma(I(w)) + k_r \, \mathrm{d}w} \, \mathrm{d}s,
\end{aligned}
$$

which depends on the initial value $A(0)$. If $A(0) = 0$, the latter becomes,

$$(2.18) \qquad A(0; t) = A_S(t)(\gamma(I(t)) + k_r) \int_0^t e^{-\int_s^t \gamma(I(w)) + k_r \mathrm{d}w} \, \mathrm{d}s.$$

Then, equation (2.14) is deduced from the definitions (2.8) and (2.9). The upper bound in (2.15) follows from the fact that γ is an increasing function of I and

$$
\begin{aligned}
\int_0^t e^{-\int_s^t \gamma(I(w)) + k_r \, \mathrm{d}w} \, \mathrm{d}s \leq {} & \int_0^t e^{-\int_s^t \gamma(I_{\min}) + k_r \, \mathrm{d}w} \, \mathrm{d}s = \frac{1 - e^{-(\gamma(I_{\min}) + k_r)t}}{\gamma(I_{\min}) + k_r} \\
& \leq \frac{1}{\gamma(I_{\min}) + k_r}.
\end{aligned}
$$

For a similar reason, we find $\int_0^t e^{-\int_s^t \gamma(I(w)) + k_r \, \mathrm{d}w} \, \mathrm{d}s \geq \int_0^t e^{-\int_s^t \gamma(I_{\max}) + k_r \, \mathrm{d}w} \, \mathrm{d}s = \frac{1 - e^{-(\gamma(I_{\max}) + k_r)t}}{\gamma(I_{\max}) + k_r}$. Substituting these two inequalities into (2.18) and using the definitions (2.8) and (2.9), we obtain the estimation (2.15). Finally, if $A(0) = A_0 \neq 0$, using (2.17) and (2.18), we have

$$
\begin{aligned}
(2.19) \qquad |A(A(0); t) - A(0; t)| = {} & |A(0)| \frac{1 + \tau \sigma_P I(0)}{1 + \tau \sigma_P I(t)} e^{-\int_0^t \gamma(I(w)) + k_r \, \mathrm{d}w} \\
& \leq |A(0)| \frac{1 + \tau \sigma_P I_{\max}}{1 + \tau \sigma_P I_{\min}} e^{-k_r t}.
\end{aligned}
$$

The latter converges to zero at a rate k_r, thus $A(A(0); t)$ converges to $A(0; t)$. $\square$

Based on Proposition 2.1, for large timescales, we will assume that the initial condition of the state A is zero.

7

2.4. Growth rate in the raceway pond. To estimate the growth rate in the raceway pond, we need to define the average growth rate of all simulated particles moving within the photobioreactor. We first define the time-averaged dynamic growth rate and its static approximation by

(2.20) $$\bar{\mu}_A := \frac{1}{T} \int_0^T \mu_A(t)\,\mathrm{d}t, \quad \bar{\mu}_S := \frac{1}{T} \int_0^T \mu_S(t)\,\mathrm{d}t.$$

Then the space-time-averaged dynamic growth rate and its static approximation are defined as

(2.21) $$\bar{\bar{\mu}}_A = \frac{1}{N_{\mathrm{par}}} \sum_{n=1}^{N_{\mathrm{par}}} \bar{\mu}_A(I_n), \quad \bar{\bar{\mu}}_S = \frac{1}{N_{\mathrm{par}}} \sum_{n=1}^{N_{\mathrm{par}}} \bar{\mu}_S(I_n).$$

In the Eulerian description, the static approximation of the growth rate μ_S can be computed for each point in the raceway domain Ω. At each point $(x, y, z) \in \Omega$, the perceived light is computed using (2.5) as $I(x, y, z) = I_0 e^{-\xi(\eta(t,x,y)-z)}$, and the volume-averaged growth rate can be defined by

(2.22) $$\bar{\bar{\mu}}_\Omega = \frac{1}{V(\Omega)} \int_\Omega \mu_S(I(x, y, z))\,\mathrm{d}x\mathrm{d}y\mathrm{d}z,$$

where $V(\Omega)$ is the volume of the raceway. In [16], the static approximation $\bar{\bar{\mu}}_S$ is used to compute the growth rate in a raceway pond. In [29], the relationship between $\bar{\bar{\mu}}_S$ and $\bar{\bar{\mu}}_\Omega$ is discussed in a different type of photobioreactor. We focus on a more accurate computation of the growth rate using $\bar{\bar{\mu}}_A$ and characterize the gain compared to the static approximation computed with $\bar{\bar{\mu}}_S$.

Instead of analyzing the flow of microalgae cells at a fixed location (Eulerian perspective), tracking Lagrangian trajectories provides a natural approach to monitor the light exposure perceived by each cell. The light history derived from these trajectories is then used to compute the growth rate $\bar{\bar{\mu}}_A$. Notably, the growth rate $\bar{\bar{\mu}}_A$ cannot be defined within a Eulerian framework, as the concept of light history is lost in this perspective.

3. Formal analysis of the average growth rate.

3.1. Time-averaged growth rate. We first assess the difference between the average growth rate $\bar{\mu}_A$ and the approximation $\bar{\mu}_S$ defined in (2.20).

THEOREM 3.1. *Let I be a bounded continuous light signal perceived by a single cell. Assuming that $A(0) = 0$, for a given time period T, the time-averaged growth rate $\bar{\mu}_A$ can be written as the sum of the time-averaged static approximation $\bar{\mu}_S$, and a correction term $\bar{\mu}_H$ representing the dynamical gain due to mixing:*

(3.1) $$\bar{\mu}_A = \bar{\mu}_S + \bar{\mu}_H + \mathcal{O}(1/T),$$

where

(3.2) $$\bar{\mu}_H := \frac{1}{T} \int_0^T \frac{\mathrm{d}\mu_S(t)}{\mathrm{d}t} \phi(t)\,\mathrm{d}t, \quad \phi(t) := \int_0^t e^{-\int_s^t \gamma(I(w))+k_r\,\mathrm{d}w}\,\mathrm{d}s,$$

and $\mathcal{O}(1/T) = -\frac{\mu_S(T)}{T}\phi(T)$ which goes to zero when $T \to +\infty$.

8

268 **Interpretation of Theorem 3.1:** In a system mainly laminar, where cells stay
269 at a constant depth (or are slowly advected vertically), for which the growth rate gain
270 due to vertical mixing $\overline{\mu}_H$ is negligible, the average growth rate over a sufficiently long
271 time period T can be accurately computed using the static approximation $\overline{\mu}_S$ based
272 on the Haldane model. In a system with high velocities in the direction of the light
273 gradient, this approximation must be refined.

274 *Proof.* Using (2.14) and integration by parts, we find

$$
\begin{aligned}
\int_0^T \mu_A(t)\mathrm{d}t &= \int_0^T \mu_S(t)(\gamma(I(t)) + k_r)\int_0^t e^{-\int_s^t \gamma(I(w)) + k_r\,\mathrm{d}w}\,\mathrm{d}s\mathrm{d}t \\
&= \int_0^T \int_s^T \mu_S(t)(\gamma(I(t)) + k_r)e^{-\int_s^t \gamma(I(w)) + k_r\,\mathrm{d}w}\,\mathrm{d}t\mathrm{d}s \\
&= \int_0^T \mu_S(s) - \mu_S(T)e^{-\int_s^T \gamma(I(w)) + k_r\,\mathrm{d}w}\,\mathrm{d}s \\
&\quad + \int_0^T \int_s^T \frac{\mathrm{d}\mu_S(t)}{\mathrm{d}t}e^{-\int_s^t \gamma(I(w)) + k_r\,\mathrm{d}w}\,\mathrm{d}t\mathrm{d}s.
\end{aligned}
$$

276 Dividing the latter by T, we get (3.1). Moreover, for a given time period T, the
277 function ϕ defined in (3.2) can be upper bounded by

278 (3.3) $$\phi(T) \le \int_0^T e^{-(\gamma(I_{\min})+k_r)(T-s)}\,\mathrm{d}s = \frac{1 - e^{-(\gamma(I_{\min})+k_r)T}}{\gamma(I_{\min}) + k_r},$$

279 and lower bounded by

280 (3.4) $$\phi(T) \ge \int_0^T e^{-(\gamma(I_{\max})+k_r)(T-s)}\,\mathrm{d}s = \frac{1 - e^{-(\gamma(I_{\max})+k_r)T}}{\gamma(I_{\max}) + k_r}.$$

281 This reveals the fact that $\mathcal{O}(1/T) \to 0$ as $T \to \infty$. $\square$

282 Note that $|\mathcal{O}(1/T)| \le \frac{\mu_{\max}}{T}\frac{1}{\gamma(I_{\min})+k_r} \le \frac{\mu_{\max}}{T}\frac{1}{k_r}$. Then, for $T \gg 1/k_r$, we can
283 approximate $\overline{\mu}_A$ by $\overline{\mu}_S + \overline{\mu}_H$, where $\overline{\mu}_H$ is defined in (3.2). The quantity $1/k_r$ cor-
284 responds to the time needed to go from the state C to B in the Han model, and
285 $T \gg 1/k_r$ means that the period T must be large enough to incorporate the effect of
286 recovery.

287 **3.2. Space-time-averaged growth rate.** We discuss here how the hydrody-
288 namics of the raceway pond affects the growth rate $\overline{\overline{\mu}}_A$ defined in (2.21). For each
289 particle, the velocity in the z-axis is given by (2.4), *i.e.*, $v_z(t, \boldsymbol{X}_n) = \boldsymbol{U}_w(\boldsymbol{X}_n(t))$. The
290 next proposition relates the velocity of the z-axis and the growth rate $\overline{\overline{\mu}}_A$.

291 PROPOSITION 3.2. *The space-time-averaged dynamic growth rate can be bounded*
292 *by the average velocity v_z in the z-axis as*

293 (3.5) $$\overline{\overline{\mu}}_A \le \overline{\overline{\mu}}_S + \frac{\alpha\xi\sigma_P I_0}{k_r}\frac{1}{N_{\mathrm{par}}}\sum_{n=1}^{N_{\mathrm{par}}}\frac{1}{T}\int_0^T |v_z(t, \boldsymbol{X}_n)|\,\mathrm{d}t + \frac{\mu_{\max}}{Tk_r}.$$

294 *Proof.* For each particle $\boldsymbol{X}_n$ and its perceived light signal I_n, we have $|\overline{\mu}_H(I_n)| \le$
295 $\frac{1}{T}\int_0^T \left|\frac{\mathrm{d}\mu_S(I_n(t))}{\mathrm{d}t}\right|\phi(I_n(t))\,\mathrm{d}t = \frac{1}{T}\int_0^T \left|\frac{\mathrm{d}\mu_S(I_n(t))}{\mathrm{d}I_n}\frac{\mathrm{d}I_n(t)}{\mathrm{d}t}\right|\phi(I_n(t))\,\mathrm{d}t$. Using then the in-

9

equality (3.3), we obtain

$$\left|\overline{\mu}_H(I_n)\right| \leq \frac{1}{T}\int_0^T \left|\frac{\mathrm{d}\mu_S(I_n(t))}{\mathrm{d}I_n}\frac{\mathrm{d}I_n(t)}{\mathrm{d}t}\right| \frac{(1 - e^{-(\gamma(I_{n,\min})+k_r)t})}{\gamma(I_{n,\min})+k_r}\,\mathrm{d}t,$$

$$\leq \frac{1}{Tk_r}\int_0^T \left|\frac{\mathrm{d}\mu_S(I_n(t))}{\mathrm{d}I_n}\frac{\mathrm{d}I_n(t)}{\mathrm{d}t}\right|\,\mathrm{d}t,$$

where $I_{n,\min}$ is the minimum value of I_n in the interval $[0,T]$. From the Lambert–Beer law, we have $\frac{\mathrm{d}}{\mathrm{d}t}I_n(t) = -\xi I_0 e^{-\xi(\eta(t,x_n,y_n)-z_n)}\left(\frac{\partial\eta}{\partial t} + \frac{\partial\eta}{\partial x}v_x + \frac{\partial\eta}{\partial y}v_y - v_z\right)$. Using (2.3) in the above, the derivative w.r.t. the light is $\frac{\mathrm{d}}{\mathrm{d}t}I_n(t) = -\xi I_n v_z(t,\boldsymbol{X}_n)$. It follows that $\left|\overline{\mu}_H(I_n)\right| \leq \frac{\xi}{Tk_r}\int_0^T \left|\frac{\mathrm{d}\mu_S(I_n(t))}{\mathrm{d}I_n}I_n(t)v_z(t,\boldsymbol{X}_n)\right|\,\mathrm{d}t$. Note that $\frac{\mathrm{d}}{\mathrm{d}I}\mu_S(I) = \frac{\alpha\sigma_P\left(1-\frac{k_d}{k_r}\tau(\sigma I)^2\right)}{\left(1+\tau\sigma_P I + \frac{k_d}{k_r}\tau(\sigma I)^2\right)^2} \leq \alpha\sigma_P$. Using the latter and the fact that $I_n(t) \leq I_0$, we have $\left|\overline{\mu}_H(I_n)\right| \leq \frac{\alpha\xi\sigma_P I_0}{Tk_r}\int_0^T |v_z(t,\boldsymbol{X}_n)|\,\mathrm{d}t$. Using (3.1), we get

$$\overline{\overline{\mu}}_A = \overline{\overline{\mu}}_S + \frac{1}{N_{\mathrm{par}}}\sum_{n=1}^{N_{\mathrm{par}}} \overline{\mu}_H(I_n) - \frac{\mu_S(I_n(t))}{T}\phi(I_n(t)),$$

$$\leq \overline{\overline{\mu}}_S + \frac{1}{N_{\mathrm{par}}}\sum_{n=1}^{N_{\mathrm{par}}} |\overline{\mu}_H(I_n)| + \frac{\mu_S(I_n(t))}{T}\phi(I_n(t)),$$

$$\leq \overline{\overline{\mu}}_S + \frac{1}{N_{\mathrm{par}}}\sum_{n=1}^{N_{\mathrm{par}}} \frac{\alpha\xi\sigma_P I_0}{Tk_r}\int_0^T |v_z(t,\boldsymbol{X}_n)|\,\mathrm{d}t + \frac{\mu_{\max}}{Tk_r},$$

which proves the inequality (3.5). $\qquad\square$

Interpretation of Proposition 3.2: We can ignore the term $\mu_{\max}/T$ in (3.5) when the time period T is large enough. Then, the difference between the space-time-averaged growth rate $\overline{\overline{\mu}}_A$ and $\overline{\overline{\mu}}_S$ cannot be greater than $\frac{\alpha\xi\sigma_P I_0}{k_r}\overline{|v_z|}$ with $\overline{|v_z|} := \frac{1}{N_{\mathrm{par}}}\sum_{n=1}^{N_{\mathrm{par}}}\int_0^T |v_z(t,\boldsymbol{X}_n)|\,\mathrm{d}t$. Here, $\overline{|v_z|}$ is an indicator of how mixed the photobioreactor is on the z-axis. A non-mixed photobioreactor will have $\overline{|v_z|} = 0$, leading to no difference between $\overline{\overline{\mu}}_S$ and $\overline{\overline{\mu}}_A$. Furthermore, the value of the light extinction ξ also plays an important role. Lower values of this parameter present less variations of the light gradient inside the reactor.

3.3. Periodic light signals. When the light signal is periodic, we can be more accurate in the results presented in Theorem 3.1. Let T now be the period of the continuous light signal I perceived by the cell, we have the following result.

PROPOSITION 3.3. *Let I a continuous periodic function, i.e., $I(t+T) = I(t)$, $\forall t \in [0,+\infty)$. Then, all solutions of* (2.13) *converge to a unique periodic solution.*

Proof. The periodic solution C_p is obtained by imposing $C_p(T) = C_p(0)$ in (2.16), and we find $C_p(0) = \frac{\int_0^T \gamma(I(s))e^{-\int_s^T \gamma(I(w))+k_r\,\mathrm{d}w}\,\mathrm{d}s}{1 - e^{-\int_0^T \gamma(I(w))+k_r\,\mathrm{d}w}}$. Let C be a solution of (2.13) and $\varepsilon = C - C_p$, we have $\dot{\varepsilon} = -(\gamma(I)+k_r)\varepsilon$. The solution is given by $\varepsilon(t) = \varepsilon(0)e^{-\int_0^t \gamma(I(s))\,\mathrm{d}s}e^{-k_r t}$, which can be bounded by $|\varepsilon(t)| \leq |\varepsilon(0)|e^{-(\gamma(I_{\min})+k_r)t}$. Then ε goes to zero as t goes to ∞. $\qquad\square$

PROPOSITION 3.4 (Dynamic growth rate for periodic signal). *Let us consider a continuous periodic light signal I of period T, i.e., $I(T) = I(0)$. Then the dynamic*

growth rate μ_A associated with the only periodic solution C_p is given by:

(3.6) $$\mu_A(t) = \mu_S(t)(\gamma(I(t)) + k_r)\left[\phi(t) + \frac{\phi(T)O(T)}{1 - O(T)}\right].$$

where ϕ is given by (3.2) and $O(T) = e^{-\int_0^T \gamma(I(w)) + k_r\, \mathrm{d}w}$.

Proof. From (2.17), we have

$$\mu_A(T) = \mu_S(T)(\gamma(I(t)) + k_r)\phi(T) + \mu_A(0)\frac{I(T)}{I(0)}\frac{1 + \tau\sigma_P I(0)}{1 + \tau\sigma_P I(T)}e^{-\int_0^T \gamma(I(w)) + k_r\, \mathrm{d}w}.$$

As the function I is periodic $I(T) = I(0)$, then $C_p(T) = C_p(0)$, and the growth rate is also periodic. Imposing $\mu_A(T) = \mu_A(0)$, we obtain $\mu_A(T) = \mu_S(T)(\gamma(I(t)) + k_r)\phi(T) + \mu_A(T)e^{-\int_0^T \gamma(I(w)) + k_r\, \mathrm{d}w}$, and thus $\mu_A(T) = \mu_S(T)\dfrac{(\gamma(I(t)) + k_r)\phi(T)}{1 - e^{-\int_0^T \gamma(I(w)) + k_r\, \mathrm{d}w}}$. Substituting then into (2.14), we find (3.6). $\square$

In the same way, we obtain the following result for the time-averaged dynamic growth rate $\overline{\mu}_A$ in the periodic case.

THEOREM 3.5 (Time-averaged growth rate in the periodic case). *Considering a periodic light signal I of period T. The time-averaged dynamic growth rate $\overline{\mu}_A$ is given by:*

(3.7) $$\overline{\mu}_A = \overline{\mu}_S + \frac{1}{1 - O(T)}\left[\overline{\mu}_H + \frac{O(T)}{T}\int_0^T \phi(T) - \phi(t)\, \mathrm{d}t\right].$$

Interpretation of Theorem 3.5: This theorem clarifies the results of Theorem 3.1, and better characterizes the dynamical component of the growth rate $\overline{\mu}_H$ which must be added to the static approximation $\overline{\mu}_S$ when the velocities along the light gradient are marked.

Proof. The proof follows the same steps as in Theorem 3.1 using the dynamic growth rate computed in the periodic case (3.6). $\square$

Note that when T is large enough, meaning that $T \gg 1/k_r$, $O(T) \to 0$, leading again to the same approximation in the non-periodic case, *i.e.*, $\overline{\mu}_A \approx \overline{\mu}_S + \overline{\mu}_H$.

3.4. Characterization of the dynamical component $\overline{\mu}_H$ as a function of the light regime. We have already seen that the actual time-averaged growth rate can be approximated by $\overline{\mu}_A \approx \overline{\mu}_S + \overline{\mu}_H$, and $\overline{\mu}_H + \mathcal{O}(1/T)$ goes to zero as the period T goes to ∞. In other words, $\overline{\mu}_S$ becomes an accurate approximation for large period T, *i.e.*, for slow movement against the light gradient. In this section, we provide a lower and upper bounds for $\overline{\mu}_H$ to understand its relationship with the variation rate of the light signal I.

PROPOSITION 3.6. *Let $I : [0, T] \to [0, +\infty)$ be a light signal of class $\mathcal{C}^1$, such that $I_{\min} \leq I(t) \leq I_{\max}, \forall t \in [0, T]$. Assume that all the stationary points of the function $t \mapsto \mu_S(I(t))$ are isolated. For $\{t_i\}_{i=0}^m$ a partition of $[0, T]$, where $t_0 = 0$, $t_m = T$, and $\frac{\mathrm{d}\mu_S(I(t_i))}{\mathrm{d}t} = 0$, then*

(3.8) $$-\frac{\mu_{\max}}{T}\frac{|\mathcal{I}_-|}{\gamma(I_{\max}) + k_r} \leq \overline{\mu}_H \leq \frac{\mu_{\max}}{T}\frac{|\mathcal{I}_+|}{\gamma(I_{\min}) + k_r},$$

11

where $|\mathcal{I}_+|$ and $|\mathcal{I}_-|$ are the cardinality of the sets:

$$\mathcal{I}_+ := \left\{ i : \frac{\mathrm{d}\mu_S(I(t))}{\mathrm{d}t} > 0 \; \forall t \in (t_i, t_{i+i}) \right\}, \; \mathcal{I}_- := \left\{ i : \frac{\mathrm{d}\mu_S(I(t))}{\mathrm{d}t} < 0 \; \forall t \in (t_i, t_{i+i}) \right\}.$$

Proof. According to the definition of $|\mathcal{I}_+|$ and $|\mathcal{I}_-|$, $\overline{\mu}_H$ can be decomposed into positive and negative parts as $\overline{\mu}_H = \overline{\mu}_H^+ + \overline{\mu}_H^-$, where $\overline{\mu}_H^+ := \frac{1}{T} \sum_{i \in \mathcal{I}_+} \int_{t_i}^{t_{i+1}} \frac{\mathrm{d}\mu_S(t)}{\mathrm{d}t} \phi(t) \mathrm{d}t$ and $\overline{\mu}_H^- := \frac{1}{T} \sum_{i \in \mathcal{I}_-} \int_{t_i}^{t_{i+1}} \frac{\mathrm{d}\mu_S(t)}{\mathrm{d}t} \phi(t) \mathrm{d}t$. Now, we can give an upper bound for the positive part $\overline{\mu}_H^+$ using (3.3),

$$\overline{\mu}_H^+ \leq \frac{1}{T} \frac{1}{\gamma(I_{\min}) + k_r} \sum_{i \in \mathcal{I}_+} \int_{t_i}^{t_{i+1}} \frac{\mathrm{d}\mu_S(t)}{\mathrm{d}t} \mathrm{d}t = \frac{1}{T} \frac{1}{\gamma(I_{\min}) + k_r} \sum_{i \in \mathcal{I}_+} \mu_S(t_{i+1}) - \mu_S(t_i).$$

In the same way, we can give a lower bound for the negative part using (3.4),

$$\overline{\mu}_H^- \geq \frac{1}{T} \frac{1}{\gamma(I_{\max}) + k_r} \sum_{i \in \mathcal{I}_-} \int_{t_i}^{t_{i+1}} \frac{\mathrm{d}\mu_S(t)}{\mathrm{d}t} \mathrm{d}t = \frac{1}{T} \frac{1}{\gamma(I_{\max}) + k_r} \sum_{i \in \mathcal{I}_-} \mu_S(t_{i+1}) - \mu_S(t_i).$$

Note that $\overline{\mu}_H^- \leq \overline{\mu}_H \leq \overline{\mu}_H^+$ due to the sign of each term. Then, using the lower bound of $\overline{\mu}_H^-$ and the upper bound of $\overline{\mu}_H^+$, we find $\frac{1}{T} \frac{\sum_{i \in \mathcal{I}_-} \mu_S(t_{i+1}) - \mu_S(t_i)}{\gamma(I_{\max}) + k_r} \leq \overline{\mu}_H \leq \frac{1}{T} \frac{\sum_{i \in \mathcal{I}_+} \mu_S(t_{i+1}) - \mu_S(t_i)}{\gamma(I_{\min}) + k_r}$. Then, as $\mu_S(t_{i+1}) - \mu_S(t_i) \leq \mu_{\max}$, we have $-\frac{1}{T} \frac{\sum_{i \in \mathcal{I}_-} \mu_{\max}}{\gamma(I_{\max}) + k_r} \leq \overline{\mu}_H \leq \frac{1}{T} \frac{\sum_{i \in \mathcal{I}_+} \mu_{\max}}{\gamma(I_{\min}) + k_r}$. $\quad\square$

Interpretation of Proposition 3.6: A particle in a constantly mixed photobioreactor cannot remain at the same depth. Therefore, the perceived light intensity I cannot be constant in any interval, and the function $t \mapsto \mu_S(I(t))$ can only have isolated stationary points. The value of $\overline{\mu}_H$ is bounded by the number of times the derivative of $\mu_S(I(t))$ changes its sign. If I is a periodic function as the one analyzed in Section 3.3, then the two sums $\sum_{i \in \mathcal{I}_+} \mu(t_{i+1}) - \mu(t_i)$ and $\sum_{i \in \mathcal{I}_-} \mu(t_{i+1}) - \mu(t_i)$ are independent of T. And if $T \to +\infty$, then $\overline{\mu}_H$ converges to 0.

An efficient trajectory for a microalgae maximizes $\overline{\mu}_H$, *i.e.*, increases growth rate due to fast changes of light along the light gradient. So, the question is which type of perceived light signals provide a higher value of $\overline{\mu}_H$. To address this point, we give a lower bound for $\overline{\mu}_H^+$:

$$\overline{\mu}_H^+ = \frac{1}{T} \sum_{i \in \mathcal{I}_+} \int_{t_i}^{t_{i+1}} \frac{\mathrm{d}\mu_S(I(t))}{\mathrm{d}t} \int_0^t e^{-\int_s^t \gamma(I(w)) + k_r \, \mathrm{d}w} \, \mathrm{d}s \mathrm{d}t$$

$$\geq \frac{1}{T} \sum_{i \in \mathcal{I}_+} \int_{t_i}^{t_{i+1}} \frac{\mathrm{d}\mu_S(I(t))}{\mathrm{d}t} \int_0^{t_i} e^{-(\gamma(I_{\max})) + k_r)(t_{i+1} - s)} \, \mathrm{d}s \mathrm{d}t,$$

$$= \frac{1}{T} \sum_{i \in \mathcal{I}_+} \frac{\delta_i}{\gamma(I_{\max}) + k_r} (\mu_S(I(t_{i+1})) - \mu_S(I(t_i))),$$

where $\delta_i = e^{-(\gamma(I_{\max}) + k_r)(t_{i+1} - t_i)} (1 - e^{-(\gamma(I_{\max}) + k_r)t_i})$.

The quantity $\overline{\mu}_H$ is instrumental to understand how growth $\overline{\mu}_A$ is stimulated in a photobioreactor by the frequent oscillations along the light gradient. This key observation will be determinant for the design and operation of photobioreactors. If

we compute $\overline{\mu}_H$ for different mixing strategies, it will inform about the most efficient mixing strategy for growth. An increase in the value of $\overline{\mu}_H$ results from higher $\overline{\mu}_H^+$ and $\overline{\mu}_H^-$. To increase the value of $\overline{\mu}_H^+$, we can look at the value of $\delta_i(\mu_S(I(t_{i+1}))-\mu_S(I(t_i)))$. The value of δ_i is larger for a shorter time interval (t_i, t_{i+1}), *i.e.*, for faster movements along the light gradient. Then, each short interval where the value $\mu_S(I(t_i))$ moves to a higher value $\mu_S(I(t_{i+1}))$ helps to increase the value of $\overline{\mu}_H^+$, and consequently, increase the value of $\overline{\mu}_A$. Although computing $\overline{\mu}_H$ is challenging, the previous observation offers a key insight to optimize productivity in a photobioreactor. In the particular case of the raceway pond, Equation (3.8) can be used to get the bound:

$$-\frac{\mu_{\max}}{T}\frac{1}{N_{\mathrm{par}}}\sum_{n=1}^{N_{\mathrm{par}}}\frac{|\mathcal{I}_-(I_n)|}{\gamma(I_{\max})+k_r} \leq \frac{1}{N_{\mathrm{par}}}\sum_{n=1}^{N_{\mathrm{par}}}\overline{\mu}_H(I_n) \leq \frac{\mu_{\max}}{T}\frac{1}{N_{\mathrm{par}}}\sum_{n=1}^{N_{\mathrm{par}}}\frac{|\mathcal{I}_+(I_n)|}{\gamma(I_{\min})+k_r}.$$

The quantity $\frac{1}{N_{\mathrm{par}}}\sum_{n=1}^{N_{\mathrm{par}}}|\mathcal{I}_-(I_n)|$ represents the average number of visits below the depth z_{opt}. In the same way, the quantity $\frac{1}{N_{\mathrm{par}}}\sum_{n=1}^{N_{\mathrm{par}}}|\mathcal{I}_+(I_n)|$ represents the average number of potential visits above the optimal depth z_{opt} (see *e.g.*, Figure 4.4). The above bounds are not tight and they provide a potential for growth enhancement if vertical hydrodynamics is sufficiently efficient.

4. Numerical study.

4.1. Periodic sketchy examples. For the numerical test, we chose the parameter values of the Han model from [13] as shown in Figure 2.3. To illustrate the behavior of the dynamic growth rate, and specifically to compare it with the static one, we consider two examples of periodic light signals. We first consider a simple periodic function for the depth of a cell

(4.1)
$$z(t) = \frac{H_0}{2}\left(1 + \sin\left(\frac{2\pi}{T}t\right)\right).$$
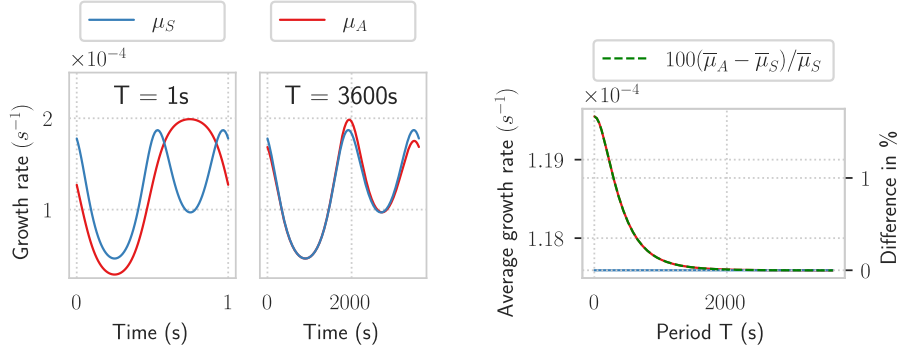
The light signal, using the Lambert–Beer law, is given by $I(t) = I_0 e^{-\xi z(t)}$ and the static approximation of the growth rate is $\mu_S(t) = \mu_S(I(t))$. In this case, the value of $\overline{\mu}_S$ is independent of T using a change of variable $s = t/T$,

$$\overline{\mu}_S = \frac{1}{T}\int_0^T \mu_S(I(t))\mathrm{d}t = \int_0^1 \frac{\alpha\sigma_P I_0 e^{-\xi z(s)}}{1 + \tau\sigma_P I_0 e^{-\xi z(s)} + \frac{k_d}{k_r}\tau\left(\sigma_P I_0 e^{-\xi z(s)}\right)^2}\mathrm{d}s.$$

In Figure 4.1a, μ_A is illustrated for the periodic solution given by (3.6). As expected, for T large enough, the difference $\overline{\mu}_A - \overline{\mu}_S$ can be approximated by $\overline{\mu}_H$. Numerically, the value of $\overline{\mu}_H$ is close to zero. In fact, their relative difference in percentage, computed as $100 \times \frac{\overline{\mu}_A - \overline{\mu}_S}{\overline{\mu}_S}$, is lower than 2%, as illustrated in Figure 4.1b. As shown in the same figure, $\overline{\mu}_A$ is always greater than $\overline{\mu}_S$ and the difference between them becomes smaller as T increases. When light varies slower, the approximation $\overline{\mu}_S$ for $\overline{\mu}_A$ is still accurate.

The actual growth rate μ_A is not always greater than the static approximation μ_S as it is shown in the second example,

(4.2)
$$z(t) = H_0 - 4H_0 \frac{e^{-\left(\sin\left(\frac{2\pi t}{T}\right)-\frac{1}{2}\right)}}{\left(1 + e^{-\left(\sin\left(\frac{2\pi t}{T}\right)-\frac{1}{2}\right)}\right)^2},$$
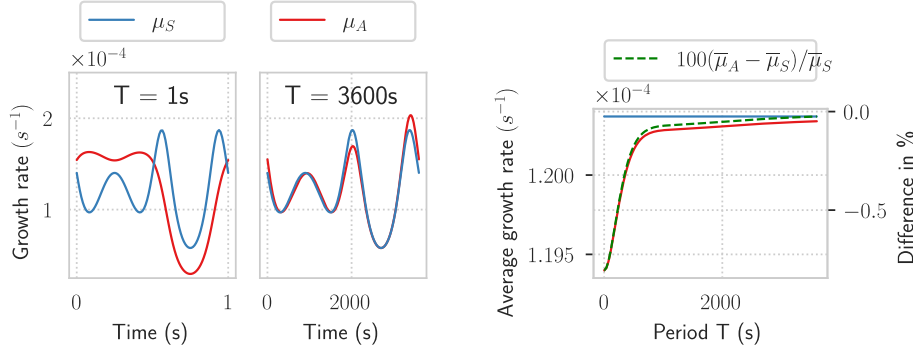
13

(a) The growth rate μ_A (in red) and the static approximation μ_S (in blue) for two different values of T. As T increases, μ_A approaches to μ_S.

(b) Time-averaged growth rate $\overline{\mu}_A$ (continuous red line) and static approximation $\overline{\mu}_S$ (blue line) for different values of T. The dashed green line shows the difference in percentage.

Fig. 4.1: Dynamic growth rate and static approximation comparison when the light signal is given by (4.1).

which also has a period T. This function describes a movement closer to the surface and does not travel to the deepest part of the culture as in (4.1). By doing the same change of variable as above, the time-averaged static approximation $\overline{\mu}_S$ is still independent of T. Similarly to Figure 4.1b, Figure 4.2b also shows the convergence of $\overline{\mu}_A$ to $\overline{\mu}_S$ when T goes to ∞. The difference in percentage between $\overline{\mu}_S$ and $\overline{\mu}_A$ is greater than in the first example. Moreover, unlike in Figure 4.1b, the value of $\overline{\mu}_A$ in Figure 4.2b is always lower than the value of $\overline{\mu}_S$. For both examples, we use $H_0 = 0.3$m and $I_0 = 1200$m$^{-2}\mu$mol.

As predicted in Proposition 3.3, for both examples, the estimation of the actual growth rate μ_A converges to μ_S (see Figure 4.1a and Figure 4.2a) as $T \to \infty$. Mixing effects are seen when the period is lower than 1500 (s). The first example shows how mixing can increase the growth rate, while the second can decrease it. Figure 4.3 presents the cell trajectories in each case. In the second example, the trajectory remains above the optimal depth, *i.e.*, in the photoinhibited part of the reactor. In this case, the effects of photoinhibition are enhanced by mixing, which explains the decrease in growth rate. However, the growth rate in the second example is still greater than in the first example. Above all, the second case represents a trajectory staying above the optimal light for growth, which means that, in the photobioreactor, other trajectories will always stay below this threshold, so that the resulting overall average growth rate is likely to be low. In conclusion, it is difficult to find an optimal mixing pattern that meets several criteria at the same time. In addition, due to the incompressibility of the fluid, leading to particle equidistribution, the trajectories of all cells fully explore the space. Only CFD simulation can eventually reconstruct realistic light patterns.

14

(a) The growth rate μ_A (in red) and the static approximation μ_S (in blue) for two different values of T. As T increases, μ_A approaches to μ_S.

(b) Time-averaged growth rate $\overline{\mu}_A$ (continuous red line) and static approximation $\overline{\mu}_S$ (blue line) for different values of T. The dashed green line shows the difference in percentage.

Fig. 4.2: Dynamic growth rate and static approximation comparison when the light signal is given by (4.2).
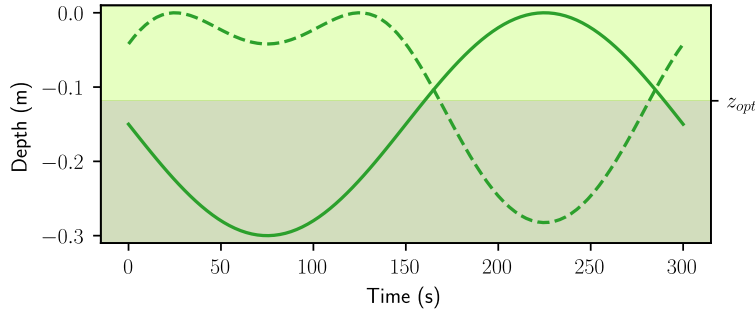

Fig. 4.3: Cell trajectories for two typical examples. The continuous line represents the trajectory given by (4.1) and the dashed line represents the trajectory associated with (4.2).

4.2. CFD simulations in the raceway pond. To account for more realistic light signals, we investigate light driven by the hydrodynamics. Figure 4.4 illustrates the tracking of a single cell within a simulated raceway pond. We use the *Freshkiss3D* Python library for the CFD simulation. We distinguish two areas within the photobioreactor: the photoinhibited section (light green) where the light perceived is greater than the optimal light I_{opt} defined in (2.10), and the photolimited section (dark green) where the light perceived is lower than I_{opt}. We denote by z_{opt} the optimal depth, which corresponds to the depth at which the algae perceive the light I_{opt} given by $z_{\mathrm{opt}} = \frac{1}{\xi} \ln\left(\frac{I_0}{I_{\mathrm{opt}}}\right)$. When the particle travels from the photolimited
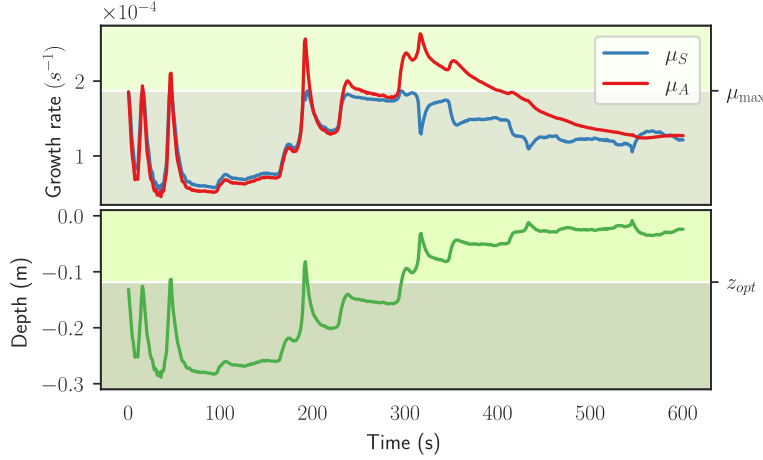
15

Fig. 4.4: Actual growth rate μ_A and static approximation μ_S for a simulated trajectory in a raceway pond operated at 20 RPM with an initial water height 0.3 (m). The maximum value of the function μ_S is denoted by $\mu_{\max}$ and the depth at which this value is reached by z_{opt}.

area to the photoinhibited area, crossing z_{opt}, the difference between μ_S and μ_A is more observable. This occurs when the particle moves faster on the z-axis than the photoinhibition mechanism. In this case, the actual growth rate μ_A could reach larger values than the estimation from the static approximation μ_S. When the cell does not go through this section fast enough, then μ_S can accurately approximate μ_A.

To account for the entire raceway system, we simulate 8 different hydrodynamical conditions by changing the velocity of the paddle wheel for a simulated time of one hour. The initial positions of the particles (x_{n0}, y_{n0}, z_{n0}) are randomly generated following an independent uniform distribution $x_{n0} \sim \mathcal{U}_{[x_{\min}, x_{\max}]}$, $y_{n0} \sim \mathcal{U}_{[y_{\min}, y_{\max}]}$, $z_{n0} \sim \mathcal{U}_{[z_{\min}, z_{\max}]}$, where the volume is defined by $B := [x_{\min}, x_{\max}] \times [y_{\min}, y_{\max}] \times [z_{\min}, z_{\max}]$ such that $\Omega \subset B$, *i.e.*, we ignore the particles outside the domain Ω of the raceway pond. Due to this process, the simulations have a slightly different number of simulated particles N_{par}. The table on the right of Figure 4.5 shows the number of simulated particles for each simulation and the total CPU time. The software *Freshkiss3D* solves (2.1) to get the velocity field, at the same time it tracks the trajectories of particles by solving (2.4). The experiments were carried out on a computer with an Intel Xeon w-2223 processor running at 1200 MHz with a total of 15677 MB of RAM and Fedora version 39.

The set of particles necessary to estimate accurately $\overline{\overline{\mu}}_A$ and $\overline{\overline{\mu}}_S$ should be representative of the entire raceway pond, meaning that the distribution should be uniform, at least on the z-axis. As experimentally validated and confirmed by simulations, perfect mixing is reached in the raceway, even at the slowest velocities. In theory, due to the incompressibility of the fluid, all biochemical quantities should be uniformly distributed. An initial uniform distribution is imposed here, but after some time, the numerical error tends to accumulate turn after turn, and particles' distribution becomes higher both in the upper and lower layers. The particles' distribution progressively drifts from equidistribution to a distribution with two pics. This error is

16

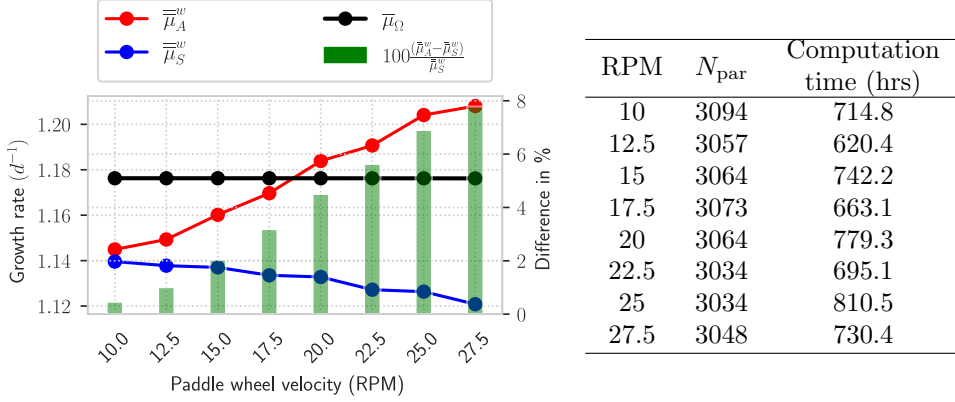| RPM	N_{par}	Computation time (hrs)
10	3094	714.8
12.5	3057	620.4
15	3064	742.2
17.5	3073	663.1
20	3064	779.3
22.5	3034	695.1
25	3034	810.5
27.5	3048	730.4

Fig. 4.5: **Left:** Growth rate of the raceway simulated for 8 different velocities of the paddle wheel in Revolutions Per Minutes (RPM). In red, the growth rate $\overline{\overline{\mu}}_A^w$ and in blue, its static approximation $\overline{\overline{\mu}}_S^w$. In black, the growth rate computed with the volume defined by the free surface $\overline{\overline{\mu}}_\Omega$. In green, the difference between them in percentage. **Right:** Computation time in hrs and the number of simulated particles for each velocity.

difficult to track, it results from the numerical approximations for solving Navier–Stokes equations, together with the numerical error when tracking each single cell in the Lagrangian approach. More particles could be simulated to mitigate this bias, but this is very CPU intensive and time consuming as shown in Figure 4.5.

Another approach consists in correcting the particles' distribution, so that the set of particles stays equidistributed. We propose a weighted average for correcting the numerical bias in the particles' distribution and more accurately compute $\overline{\overline{\mu}}_A$ and $\overline{\overline{\mu}}_S$,

$$\overline{\overline{\mu}}_A^w = \frac{1}{T} \int_0^T \frac{\sum_{n=1}^{N_{par}} \frac{\mu_A(I_n(t))}{h(t,\mathbf{X}_n)}}{\sum_{n=1}^{N_{par}} \frac{1}{h(t,\mathbf{X}_n)}} \, dt \quad \text{and} \quad \overline{\overline{\mu}}_S^w = \frac{1}{T} \int_0^T \frac{\sum_{n=1}^{N_{par}} \frac{\mu_S(I_n(t))}{h(t,\mathbf{X}_n)}}{\sum_{n=1}^{N_{par}} \frac{1}{h(t,\mathbf{X}_n)}} \, dt.$$

Here, $\mu_A(I_n(\cdot))$ and $\mu_S(I_n(\cdot))$ are computed from the light history $I_n(\cdot)$ perceived by the algae, using (2.14) and (2.9) respectively, and $h(t,\cdot)$ is the probability density function of the depth of the particles at the instant t. If the free surface is perfectly flat with depth H_0, we have that $h(0,\cdot) = 1/H_0$ by construction (since all particles are initialized with uniform distribution on the z-axis), and we recover the expression (2.21). Figure 4.5 shows the computation of $\overline{\overline{\mu}}_A^w$ and $\overline{\overline{\mu}}_S^w$.

4.3. Approximation of the growth rate. When the particle number N_{par} is large enough, the space-time-averaged static approximation defined in (2.21) converges to the volume-averaged growth rate (2.22) in the sense that

(4.3) $$\lim_{N_{par}\to\infty} \overline{\overline{\mu}}_S(I_n) = \lim_{N_{par}\to\infty} \overline{\overline{\mu}}_S^w(I_n) = \overline{\overline{\mu}}_\Omega,$$

when the fluid is incompressible [29]. Figure 4.5 shows $\overline{\overline{\mu}}_\Omega$ computed for eight different paddle wheel velocities. We observe that this quantity is a constant independent of the simulated velocities. In fact, the volume-averaged growth rate $\overline{\overline{\mu}}_\Omega$ depends only

17

on the aquatic volume in the photobioreactor. Since the volume is constant in our numerical tests, this quantity can then be computed only considering the geometry of the raceway pond and the height of the water, making $\overline{\overline{\mu}}_\Omega$ an efficient approximation of the growth rate. Two raceway ponds with equivalent shape lead to the same volume-averaged growth rate $\overline{\overline{\mu}}_\Omega$ [20, Theorem 3]. The same holds for the corrected space-time-averaged static approximation $\overline{\overline{\mu}}_S^w$ when $N_{\mathrm{par}} \to \infty$. And in the limit case, $\overline{\overline{\mu}}_S^w$ no longer sees the effect of hydrodynamics. This explains the reason why $\overline{\overline{\mu}}_S^w$ has a small variation when the paddle wheel velocity changes in Figure 4.5. More precisely, the values of the corrected space-time-averaged static approximation $\overline{\overline{\mu}}_S^w$ are 1.1395 (d^{-1}) for 10 RPM and 1.12080 (d^{-1}) for 27.5 PRM. The difference between the actual growth rate computed using the dynamic description $\overline{\overline{\mu}}_A^w$ and the static approximation $\overline{\overline{\mu}}_S^w$ is lower than 8% (at 27.5 RPM). Then, the actual growth rate $\overline{\overline{\mu}}_A^w$ is almost not sensitive to the simulated velocity of the paddle wheel. In this way, it is not worthwhile to simulate hydrodynamics to obtain a more accurate measurement of the growth rate, as CFD simulations are very time consuming (see the table in Figure 4.5). Hydrodynamics have a minor effect on the overall growth rate, this conclusion is firmly related to the system presented here. A different photobioreactor could lead to different conclusions.

5. Discussion. Simulating the coupling between hydrodynamics and photosynthesis is a significant scientific challenge, involving multiple timescales and nonlinear dynamic models. In this study, we demonstrated how the average growth rate of microalgae in a bioreactor can be optimized through careful management of hydrodynamics. A key observation is that the increase in productivity is directly linked to the movement of cells along the light gradient. This dynamic movement enhances the growth rate compared to a static scenario, where cells remain immobile.

Better understanding hydrodynamics and their favorable impact on microalgae productivity paves the way for optimizing photobioreactors. In particular, it enables the design of systems capable of generating targeted movements along the light gradient, a key factor for maximizing microalgae growth. Other types of movements, while essential for ensuring mixing homogeneity, have no significant effect on productivity. Therefore, a strategic approach aimed at exploiting beneficial movements within the light gradient could significantly enhance the efficiency of microalgae cultivation. However, modeling this coupling between physics and biology presents several challenges. On one hand, the dynamics of photosynthesis in response to light fluctuations are complex to capture. Current models, which focus on the efficiency of photosystems, require more robust experimental validation [10]. On the other hand, hydrodynamic models have their own limitations, particularly when adopting a Lagrangian approach. Indeed, the property of iso-distribution of particles tends to degrade over time, an aspect often overlooked in previous studies but crucial in the context of periodic fluid circulations. To address this issue, we propose a strategy to compensate distribution biases, essential to avoid numerical drifts and erroneous conclusions.

Our study focuses on a simplified case, where we assume no cell sedimentation (*i.e.*, cell density equal to that of the fluid) and perfect adherence to streamlines. A range of biological mechanisms such as photoacclimation and photoprotection with specific pigments to cope with high light have been neglected [10]. Additionally, we neglect external light fluctuations, such as those induced by day-night cycles. Although our approach is general from a mathematical perspective, the simulations are specifically applied to high-rate ponds. Similar studies for photobioreactors could validate these mechanisms in faster hydrodynamic regimes [26], where the productivity

18

gain from cell agitation could be significantly higher than that observed in raceway ponds. Mixing can also indirectly promote growth for other reasons. On top of avoiding sedimentation, it enhances the mass transfer with gases [8], leading to higher CO_2 transfer rate or increasing O_2 outgassing, both being favorable for photosynthesis. Here, the study was carried out assuming a constant medium turbidity, *i.e.*, a constant microalgal biomass concentration. A higher growth rate would probably support a higher biomass in the reactor, reducing the average light in the reactor. This effect should be further studied with dedicated models also taking into account other timescale of the photosynthesis [24].

An important conclusion of this study is that the productivity gain associated with mixing velocity stays in the range of a few percent of the static approximation of the growth rate. This most probably explains why, despite recurrent statements in the literature [28], the increase of productivity with more intense agitation has never been clearly demonstrated experimentally. Given the high computational cost of simulating reactor hydrodynamics and tracking particles to compute the average growth rate, a correction factor applied to the growth parameter, accounting for the hydrodynamics, is probably the most efficient numerical approach. Such correction term should be calibrated on real systems, to automatically capture the photosynthesis stimulation due to the cell movement in the light field. It is crucial to balance the gain in productivity with the energy required for mixing, which increases with the cube of the fluid velocity [9, 30]. Excessive agitation could lead to disproportionate energy costs without a significant improvement in productivity [21]. These results could serve as a basis for a life cycle assessment (LCA) to determine the optimal agitation intensity, taking into account environmental and energy impacts [22]. Such an approach would help identify a trade-off between productivity and sustainability.

6. Conclusions. We presented a numerical method for calculating the average growth rate in a photobioreactor, incorporating the effects of hydrodynamics. Our approach was based on the Han model to represent the photosynthesis dynamics and account for the light history of the microalgae. By coupling the Han model with hydrodynamics, we captured the influence of mixing devices on microalgae growth. We demonstrated analytically that cell advection along the light gradient is the determining reason to stimulate photosynthesis efficiency.

We simulated the light harvesting model within the light field generated by the hydrodynamics of a raceway pond. Many publications have been dedicated to improve the mixing in photobioreactors, but the criterion of the resulting algal productivity was not taken into account. Our study opens new routes to more directly optimize bioreactor productivity through hydrodynamics management. The relationship between the growth rate in the raceway and the vertical velocity (z-axis) can be extended to other photobioreactors, depending on their hydrodynamics and internal light distribution. This insight provides a basis for optimizing the reactor geometry and mixing to maximize the benefits of hydrodynamic effects by ensuring cell movements along the light gradient.

REFERENCES

[1] ALI, H., CHEEMA, T. A., YOON, H.-S., DO, Y., AND PARK, C. W. Numerical prediction of algae cell mixing feature in raceway ponds using particle tracing methods. *Biotechnology and bioengineering 112*, 2 (2015), 297–307.

[2] ALLGEYER, S., BRISTEAU, M.-O., FROGER, D., HAMOUDA, R., JAUZEIN, V., MANGENEY, A., SAINTE-MARIE, J., SOUILLÉ, F., AND VALLÉE, M. Numerical approximation of the 3D

19

hydrostatic Navier–Stokes system with free surface. *ESAIM: Mathematical Modelling and Numerical Analysis 53*, 6 (2019), 1981–2024.

[3] BÉCHET, Q., SHILTON, A., AND GUIEYSSE, B. Modeling the effects of light and temperature on algae growth: state of the art and critical assessment for productivity prediction during outdoor cultivation. *Biotechnology advances 31*, 8 (2013), 1648–1663.

[4] BERNARD, O., BOULANGER, A.-C., BRISTEAU, M.-O., AND SAINTE-MARIE, J. A 2D model for hydrodynamics and biology coupling applied to algae growth simulations. *ESAIM: Mathematical Modelling and Numerical Analysis 47*, 5 (2013), 1387–1412.

[5] BERNARD, O., LU, L.-D., SAINTE-MARIE, J., AND SALOMON, J. Topography optimization for enhancing microalgal growth in raceway ponds. Submitted, 2024.

[6] BERNARD, O., LU, L.-D., AND SALOMON, J. Optimal periodic resource allocation in reactive dynamical systems: Application to microalgal production. *International Journal of Robust and Nonlinear Control 33*, 9 (2023), 4989–5010.

[7] BERNARD, O., MAIRET, F., AND CHACHUAT, B. Modelling of microalgae culture systems with applications to control and optimization. *Microalgae Biotechnology* (2015), 59–87.

[8] CAIA, M., BERNARD, O., AND BÉCHET, Q. Optimizing CO_2 transfer in algal open ponds. *Algal research 35* (2018), 530–538.

[9] CHIARAMONTI, D., PRUSSI, M., CASINI, D., TREDICI, M. R., RODOLFI, L., BASSI, N., ZITTELLI, G. C., AND BONDIOLI, P. Review of energy balance in raceway ponds for microalgae cultivation: Re-thinking a traditional system is possible. *Applied Energy 102* (2013), 101–111.

[10] DEMORY, D., COMBE, C., HARTMANN, P., TALEC, A., PRUVOST, E., HAMOUDA, R., SOUILLÉ, F., LAMARE, P.-O., BRISTEAU, M.-O., SAINTE-MARIE, J., ET AL. How do microalgae perceive light in a high-rate pond? towards more realistic lagrangian experiments. *Royal Society open science 5*, 5 (2018), 180523.

[11] EILERS, P., AND PEETERS, J. A model for the relationship between light intensity and the rate of photosynthesis in phytoplankton. *Ecological modelling 42*, 3-4 (1988), 199–215.

[12] FIERRO ULLOA, J. I., LU, L.-D., AND BERNARD, O. Theoretical growth rate of microalgae under high/low-flashing light. *Journal of Mathematical Biology 86*, 4 (2023), 48.

[13] GRENIER, J., LOPES, F., BONNEFOND, H., AND BERNARD, O. Worldwide perspectives of rotating algal biofilm up-scaling. Submitted paper, 2020.

[14] HAN, B.-P. A mechanistic model of algal photoinhibition induced by photodamage to photosystem-II. *Journal of theoretical biology 214*, 4 (2002), 519–527.

[15] HARTMANN, P., BÉCHET, Q., AND BERNARD, O. The effect of photosynthesis time scales on microalgae productivity. *Bioprocess and biosystems engineering 37*, 1 (2014), 17–25.

[16] HARTMANN, P., DEMORY, D., COMBE, C., HAMOUDA, R., BOULANGER, A.-C., BRISTEAU, M.-O., SAINTE-MARIE, J., SIALVE, B., STEYER, J.-P., RABOUILLE, S., ET AL. Growth rate estimation of algae in raceway ponds: A novel approach. *IFAC Proceedings Volumes 47*, 3 (2014), 6216–6221.

[17] HREIZ, R., SIALVE, B., MORCHAIN, J., ESCUDIÉ, R., STEYER, J.-P., AND GUIRAUD, P. Experimental and numerical investigation of hydrodynamics in raceway reactors used for algaculture. *Chemical Engineering Journal 250* (2014), 230–239.

[18] KHALIL, H. *Nonlinear Systems*. Pearson Education. Prentice Hall, 2002.

[19] MAGALHÃES, I. B., FERREIRA, J., DE SIQUEIRA CASTRO, J., DE ASSIS, L. R., AND CALIJURI, M. L. Agro-industrial wastewater-grown microalgae: A techno-environmental assessment of open and closed systems. *Science of The Total Environment 834* (2022), 155282.

[20] MARTÍNEZ, C., MAIRET, F., AND BERNARD, O. Theory of turbid microalgae cultures. *Journal of theoretical biology 456* (2018), 190–200.

[21] MENDOZA, J., GRANADOS, M., DE GODOS, I., ACIÉN, F., MOLINA, E., BANKS, C., AND HEAVEN, S. Fluid-dynamic characterization of real-scale raceway reactors for microalgae production. *Biomass and Bioenergy 54* (2013), 267–275.

[22] MORALES, M., COLLET, P., LARDON, L., HÉLIAS, A., STEYER, J.-P., AND BERNARD, O. Life-cycle assessment of microalgal-based biofuel. *Biofuels from algae* (2019), 507–550.

[23] NIKOLAOU, A., BOOTH, P., GORDON, F., YANG, J., MATAR, O., AND CHACHUAT, B. Multi-physics modeling of light-limited microalgae growth in raceway ponds. *IFAC-PapersOnLine 49*, 26 (2016), 324–329.

[24] NIKOLAOU, A., HARTMANN, P., SCIANDRA, A., CHACHUAT, B., AND BERNARD, O. Dynamic coupling of photoacclimation and photoinhibition in a model of microalgae growth. *Journal of theoretical biology 390* (2016), 61–72.

[25] PANDEY, R., AND PREMALATHA, M. Design and analysis of flow velocity distribution inside a raceway pond using computational fluid dynamics. *Bioprocess and Biosystems engineering 40*, 3 (2017), 439–450.

20

[26] PERNER, I., POSTEN, C., AND BRONESKE, J. CFD optimization of a plate photobioreactor used for cultivation of microalgae. *Engineering in life sciences 3*, 7 (2003), 287–291.

[27] PRUSSI, M., BUFFI, M., CASINI, D., CHIARAMONTI, D., MARTELLI, F., CARNEVALE, M., TREDICI, M. R., AND RODOLFI, L. Experimental and numerical investigations of mixing in raceway ponds for algae cultivation. *Biomass and bioenergy 67* (2014), 390–400.

[28] RICHMOND, A., Ed. *Handbook of microalgal culture: biotechnology and applied phycology*, vol. 577. Wiley Online Library, 2004.

[29] TONG, Z.-X., LI, M.-J., YAN, J.-J., AND GU, Z.-L. A theoretical analysis of the hydrodynamic influence on the growth of microalgae in the photobioreactors with simple growth kinetics. *International Journal of Heat and Mass Transfer 158* (2020), 119986.

[30] ZHU, C., JI, Y., DU, X., KONG, F., CHI, Z., AND ZHAO, Y. A smart and precise mixing strategy for efficient and cost-effective microalgae production in open ponds. *Science of the Total Environment 852* (2022), 158515.

21